The Astrophysical Journal, 793:21 (12pp), 2014 September 20 doi:10.1088/0004-637X/793/1/21

BROADBAND X-RAY SPECTRA OF THE ULTRALUMINOUS X-RAY SOURCE HOLMBERG IX X-1 OBSERVED WITH *NuSTAR*, *XMM-NEWTON,* AND *SUZAKU*

D. J. Walton[1], F. A. Harrison[1], B. W. Grefenstette[1], J. M. Miller[2], M. Bachetti[3,4], D. Barret[3,4], S. E. Boggs[5], F. E. Christensen[6], W. W. Craig[5], A. C. Fabian[7], F. Fuerst[1], C. J. Hailey[8], K. K. Madsen[1], M. L. Parker[7], A. Ptak[9], V. Rana[1], D. Stern[1,10], N. Webb[3,4], and W. W. Zhang[9]

[1] Space Radiation Laboratory, California Institute of Technology, Pasadena, CA 91125, USA; dwalton@srl.caltech.edu
[2] Department of Astronomy, University of Michigan, 500 Church Street, Ann Arbor, MI 48109-1042, USA
[3] Universite de Toulouse, UPS-OMP, IRAP, Toulouse, France
[4] CNRS, IRAP, 9 Av. colonel Roche, BP 44346, F-31028 Toulouse cedex 4, France
[5] Space Sciences Laboratory, University of California, Berkeley, CA 94720, USA
[6] DTU Space, National Space Institute, Technical University of Denmark, Elektrovej 327, DK-2800 Lyngby, Denmark
[7] Institute of Astronomy, University of Cambridge, Madingley Road, Cambridge CB3 0HA, UK
[8] Columbia Astrophysics Laboratory, Columbia University, New York, NY 10027, USA
[9] NASA Goddard Space Flight Center, Greenbelt, MD 20771, USA
[10] Jet Propulsion Laboratory, California Institute of Technology, Pasadena, CA 91109, USA
Received 2014 February 11; accepted 2014 July 7; published 2014 August 29

ABSTRACT

We present results from the coordinated broadband X-ray observations of the extreme ultraluminous X-ray source Holmberg IX X-1 performed by *NuSTAR*, *XMM-Newton*, and *Suzaku* in late 2012. These observations provide the first high-quality spectra of Holmberg IX X-1 above 10 keV to date, extending the X-ray coverage of this remarkable source up to ∼30 keV. Broadband observations were undertaken at two epochs, between which Holmberg IX X-1 exhibited both flux and strong spectral variability, increasing in luminosity from $L_{\rm X} = (1.90 \pm 0.03) \times 10^{40}$ erg s^{-1} to $L_{\rm X} = (3.35 \pm 0.03) \times 10^{40}$ erg s^{-1}. Neither epoch exhibits a spectrum consistent with emission from the standard low/hard accretion state seen in Galactic black hole binaries, which would have been expected if Holmberg IX X-1 harbors a truly massive black hole accreting at substantially sub-Eddington accretion rates. The *NuSTAR* data confirm that the curvature observed previously in the 3–10 keV bandpass does represent a true spectral cutoff. During each epoch, the spectrum appears to be dominated by two optically thick thermal components, likely associated with an accretion disk. The spectrum also shows some evidence for a nonthermal tail at the highest energies, which may further support this scenario. The available data allow for either of the two thermal components to dominate the spectral evolution, although both scenarios require highly nonstandard behavior for thermal accretion disk emission.

Key words: black hole physics – X-rays: binaries – X-rays: individual (Holmberg IX X-1)

Online-only material: color figures

1. INTRODUCTION

Ultraluminous X-ray sources (ULXs) are off-nuclear point sources with X-ray luminosities $L_{\rm X} > 10^{39}$ erg s^{-1}, in excess of the Eddington limit for the typical 10 $M_{\odot}$ stellar-remnant black holes observed in Galactic black hole binaries (BHBs; e.g., Orosz 2003). Multi-wavelength observations have largely excluded strong anisotropic emission as a means of substantially skewing luminosity estimates (e.g., Berghea et al. 2010; Moon et al. 2011), thus these high luminosities require either the presence of larger black holes, either stellar remnant black holes more massive than observed in our own Galaxy (e.g., Zampieri & Roberts 2009) or perhaps even the long postulated "intermediate mass" black holes (IMBHs: $10^2 \lesssim M_{\rm BH} \lesssim 10^5\,M_{\odot}$, e.g., Miller et al. 2004; Strohmayer & Mushotzky 2009), or exotic super-Eddington modes of accretion (e.g., Poutanen et al. 2007; Finke & Böttcher 2007). The majority of ULXs only radiate marginally in excess of 10^{39} erg s^{-1} (Walton et al. 2011b; Swartz et al. 2011), and are likely to simply represent a high luminosity extension of the stellar mass BHB population (Middleton et al. 2013; Liu et al. 2013). Of particular interest are the rare population of extreme ULXs with X-ray luminosities $L_{\rm X} > 10^{40}$ erg s^{-1} (e.g., Farrell et al. 2009; Walton et al. 2011b, 2013a; Jonker et al. 2012; Sutton et al. 2012). The extreme luminosities displayed by these sources make them the best candidates for hosting more massive black holes. For recent reviews on the observational status and the potential nature of ULXs, see Roberts (2007) and Feng & Soria (2011).

Previous studies have established that the 0.3–10.0 keV X-ray spectra of these extreme ULXs typically show evidence for two separate continuum components (e.g., Miller et al. 2003; Vierdayanti et al. 2010; Miller et al. 2013b), one dominating at softer ($\lesssim$2 keV) and the other at harder X-rays ($\gtrsim$2 keV), potentially analogous to the disk–corona accretion components inferred for sub-Eddington BHBs (see Remillard & McClintock 2006 for a review). However, studies focusing on the highest signal-to-noise data have found that the harder component generally shows evidence of subtle curvature in the ∼3–10 keV bandpass (Stobbart et al. 2006; Gladstone et al. 2009; Walton et al. 2011a), which is not observed in the coronal emission of standard sub-Eddington accretion states. A number of interpretations have since been proposed for this spectral structure, which can broadly be grouped into those that invoke thermal processes for the harder component (e.g., emission from a hot accretion disk; Gladstone et al. 2009; Middleton et al. 2011b; Sutton et al. 2013), which generally invoke super-Eddington accretion, and those that invoke nonthermal processes (e.g., a combination of a power-law continuum and relativistic reflection from the inner disk; Caballero-García & Fabian 2010), which may

still involve intermediate mass black holes (IMBHs; $M_{\rm BH} \sim 10^{2-5}\ M_{\odot}$). As demonstrated in Walton et al. (2011a), these different model families predict substantially different spectra above 10 keV, in the bandpass only readily accessible with the focusing hard X-ray telescopes aboard the recently launched Nuclear Spectroscopic Telescope Array (*NuSTAR*; Harrison et al. 2013).

Holmberg IX X-1 is one of the best studied extreme ULXs, which although known to vary in flux (e.g., Kong et al. 2010; Vierdayanti et al. 2010) is one of the few sources (within $\sim$5 Mpc) to persistently radiate at $L_{\rm X} > 10^{40}$ erg s^{-1}. Early *XMM-Newton* observations revealed the possible presence of a very cool accretion disk (Miller et al. 2003), which may evolve in a fashion similar to the $L \propto T^4$ relation expected for simple blackbody radiation (Miller et al. 2013b), and indicate the presence of a massive black hole. However, as with other extreme ULXs for which high quality data are available, Holmberg IX X-1 shows evidence for high energy spectral curvature (e.g., Stobbart et al. 2006; Gladstone et al. 2009; Walton et al. 2013b). Holmberg IX X-1 is also one of the brightest ULXs in the iron K α bandpass, and sensitive searches have been made for absorption features that would be indicative of the massive outflows ubiquitously predicted by simulations of super-Eddington accretion (e.g., Ohsuga & Mineshige 2011; Dotan & Shaviv 2011). No features are detected, with limits that require that any undetected features to be weaker than the iron absorption features resulting from the outflows in a number of sub-Eddington Galactic BHBs (Walton et al. 2012, 2013b).

Reconciling these various results into a coherent picture regarding the nature of Holmberg IX X-1 remains challenging. In order to shed further light onto the nature of the accretion in this source, we undertook a series of observations with *NuSTAR* in order to determine the nature of the high energy emission. These were coordinated with *Suzaku* and/or *XMM-Newton*, providing the first high quality broadband ($\sim$0.3–30.0 keV) X-ray spectra of Holmberg IX X-1. The paper is structured as follows. Section 2 describes our data reduction procedure, and Sections 3 and 4 describe the analysis performed. We discuss our results in Section 5 and summarize our conclusions in Section 6.

2. DATA REDUCTION

Holmberg IX X-1 was observed by each of the *NuSTAR*, *XMM-Newton*, and *Suzaku* X-ray observatories on multiple occasions during 2012. The observations used in this work are summarized in Table 1. Here, we outline our data reduction for these observations.

2.1. NuSTAR

NuSTAR performed two observations of Holmberg IX X-1 in late 2012 (referred to throughout this work as epochs 1 and 2), separated by roughly two weeks (see Table 1). While the first observation (ObsIDs 30002033002 and 30002033003) was taken continuously, the second (ObsIDs 30002033005, 30002033006, 30002033008 and 30002033010) was split into three contemporaneous segments in order to maximize the overlap with our *XMM-Newton* observations (see below). We reduced the *NuSTAR* data using the standard pipeline, part of the *NuSTAR* Data Analysis Software v1.3.0 (NUSTARDAS; included in the standard HEASOFT distribution as of version 14), and we used instrumental responses from *NuSTAR* caldb v20131007 throughout. We cleaned the unfiltered event files with the standard depth correction, which significantly reduces the internal background at high energies, and removed periods of Earth occultation and passages through the South Atlantic Anomaly, which result in a typical observing efficiency of $\sim$50%. Source products were obtained from circular regions (radius $\sim$70″), and the background was estimated from a larger, blank area of the same detector free of contaminating point sources. Spectra and light curves were extracted from the cleaned event files using XSELECT for both focal plane modules (FPMA and FPMB). Finally, the spectra were grouped such that each spectral bin contains at least 50 counts. These *NuSTAR* observations provide good spectra for Holmberg IX X-1 up to $\sim$30–35 keV from each of the focal plane modules, FPMA and FPMB, for each epoch. In this work, we fit the spectra from FPMA and FPMB jointly, without combining them.

Table 1
Details of the X-Ray Observations Considered in this Work, Ordered Chronologically

Mission	ObsID	Date	Good Exposure[a] (ks)
	Epoch 1		
Suzaku	707019020	2012 Oct 21	107
XMM-Newton	0693850801	2012 Oct 23	6/10
Suzaku	707019030	2012 Oct 24	107
XMM-Newton	0693850901	2012 Oct 25	7/13
Suzaku	707019040	2012 Oct 26	110
NuSTAR	30002033002	2012 Oct 26	31
NuSTAR	30002033003	2012 Oct 26	88
XMM-Newton	0693851001	2012 Oct 27	4/13
	Epoch 2		
NuSTAR	30002033005	2012 Nov 11	41
NuSTAR	30002033006	2012 Nov 11	35
XMM-Newton	0693851701	2012 Nov 12	7/9
NuSTAR	30002033008	2012 Nov 14	15
XMM-Newton	0693851801	2012 Nov 14	7/9
NuSTAR	30002033010	2012 Nov 15	49
XMM-Newton	0693851101	2012 Nov 16	3/7

Note. [a] *XMM-Newton* exposures are listed for the *EPIC*-pn/MOS detectors, while *NuSTAR* exposures quoted are for each of the focal plane modules.

2.2. Suzaku

2.2.1. XIS Detectors

The first *NuSTAR* observation of Holmberg IX X-1 was performed simultaneously with a portion of our recent long integration (Walton et al. 2013b) with the *Suzaku* observatory (Mitsuda et al. 2007). Figure 1 highlights the relative coordination of all the observations considered in this work. The data reduction procedure for the XIS detectors (Koyama et al. 2007) for the full *Suzaku* data set, including observations taken in 2012 April, has already been described in Walton et al. (2013b), following the procedure recommended in the *Suzaku* data reduction guide.[11] Here we only consider the *Suzaku* data taken either simultaneously or contemporaneously with *NuSTAR* in October, and we re-reduce the spectra following the same procedure with the latest XIS calibration files (released 2013 September), which substantially improves the agreement between the front- and back-illuminated XIS detectors at low energies. In this work, we model the XIS data over the 0.7–10.0 keV energy range (unless stated otherwise), excluding the 1.6–2.1 keV band throughout,

[11] http://heasarc.gsfc.nasa.gov/docs/suzaku/analysis/

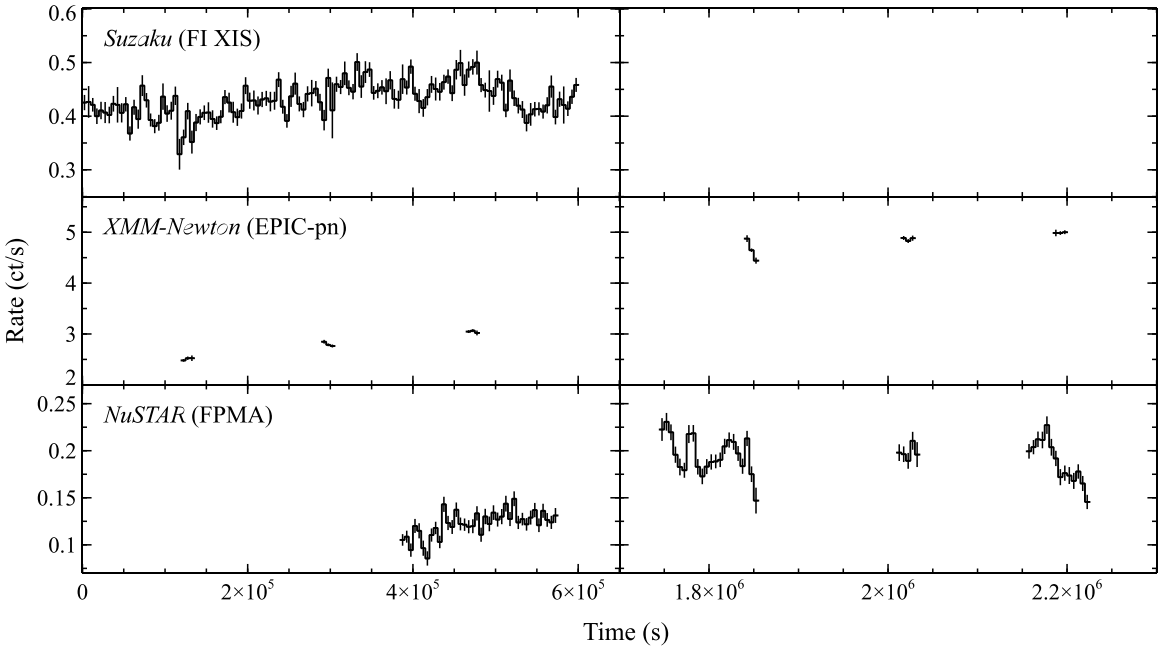

Figure 1. Light curves obtained for Holmberg IX X-1 in 5 ks bins with *Suzaku* (top panels), *NuSTAR* (middle panels), and *XMM-Newton* (bottom panels) during our observing program in late 2012, indicating the relative coordination of the various observations utilized in this work.

owing to remaining calibration uncertainties associated with the instrumental silicon K edge. We also rebin the XIS spectra to have a minimum of 50 counts per energy bin.

2.2.2. HXD PIN

Owing to the combination of the systematic uncertainty in the background model for the *Suzaku* PIN detector (Takahashi et al. 2007)—equivalent to $\gtrsim$25% of the "source" flux for the weak detection of the Holmberg IX field (see, e.g., discussion in Walton et al. 2013c)—and the source confusion resulting from its lack of imaging capability—the variable nucleus of M81 (e.g., Markoff et al. 2008; Miller et al. 2010) also falls in the PIN field-of-view—the data obtained with this detector unfortunately cannot be used to constrain the high energy ($E > 10$ keV) properties of Holmberg IX X-1 (Walton et al. 2013b). Therefore, we do not consider the PIN data here, and focus instead on the high energy data provided by *NuSTAR*.

2.3. XMM-Newton

For our *XMM-Newton* observations, data reduction was carried out with the *XMM-Newton* Science Analysis System (SAS v13.5.0) largely according to the standard prescription provided in the online guide.[12] The observation data files were processed using EPCHAIN and EMCHAIN to produce calibrated event lists for the *EPIC*-pn (Strüder et al. 2001) and *EPIC*-MOS (Turner et al. 2001) detectors, respectively. Source products were extracted from circular regions of radius $\sim$40″ for *EPIC*-pn, and of radius $\sim$50″ for the *EPIC*-MOS, selected to avoid chip gaps (where relevant). In each case the background was estimated from a larger area of the same CCD free from contaminating point sources. Light curves and spectra were generated with XMMSELECT, excluding periods of high background flares and selecting only single and double events for *EPIC*-pn, and single to quadruple events for *EPIC*-MOS during the first epoch. For the second epoch, the source was bright enough for the *EPIC*-MOS data to be affected by mild pileup, and so for these three observations we considered only single grade events in order to mitigate against these effects. The redistribution matrices and auxiliary response files were generated with RMFGEN and ARFGEN, while light curves were corrected for the background count rate using EPICLCCORR. After performing the data reduction separately for each of the MOS detectors, and confirming their consistency, these spectra were combined using the FTOOL ADDASCASPEC. Finally, spectra were rebinned using the SAS task SPECGROUP to have a minimum of 50 counts in each energy bin. The *XMM-Newton* data are modeled over the full 0.3–10.0 keV bandpass (unless stated otherwise).

[12] http://xmm.esac.esa.int/

3. SPECTRAL ANALYSIS

During these observations, Holmberg IX X-1 displayed some flux variability, both between epochs and within a single epoch (Figure 1). We therefore test to see whether this flux variability is accompanied by strong spectral variability in order to determine how to best extract spectra. In Figure 2 we show the *XMM-Newton* spectra obtained from each of the three observations associated with each epoch. Despite the mild flux variability, the spectra obtained within each epoch show good consistency. However, we do see differences in the broadband spectra when comparing epoch 1 and epoch 2. Given the lack of short-term spectral variability, we do not require strict simultaneity between *NuSTAR*, *Suzaku* and/or *XMM-Newton*. This allows us to maintain the highest S/N possible in the *NuSTAR* data, and we combine the available data from each of the missions into average spectra for each epoch, which we analyze simultaneously. However, we keep our analysis of epochs 1 and 2 separate.

We investigate the broadband spectral properties of Holmberg IX X-1 utilizing a similar suite of models to those applied in recent broadband spectral studies of other ULXs (Walton et al. 2013a; Bachetti et al. 2013; Rana et al. 2014). Throughout this work, spectral modeling is performed with XSPEC

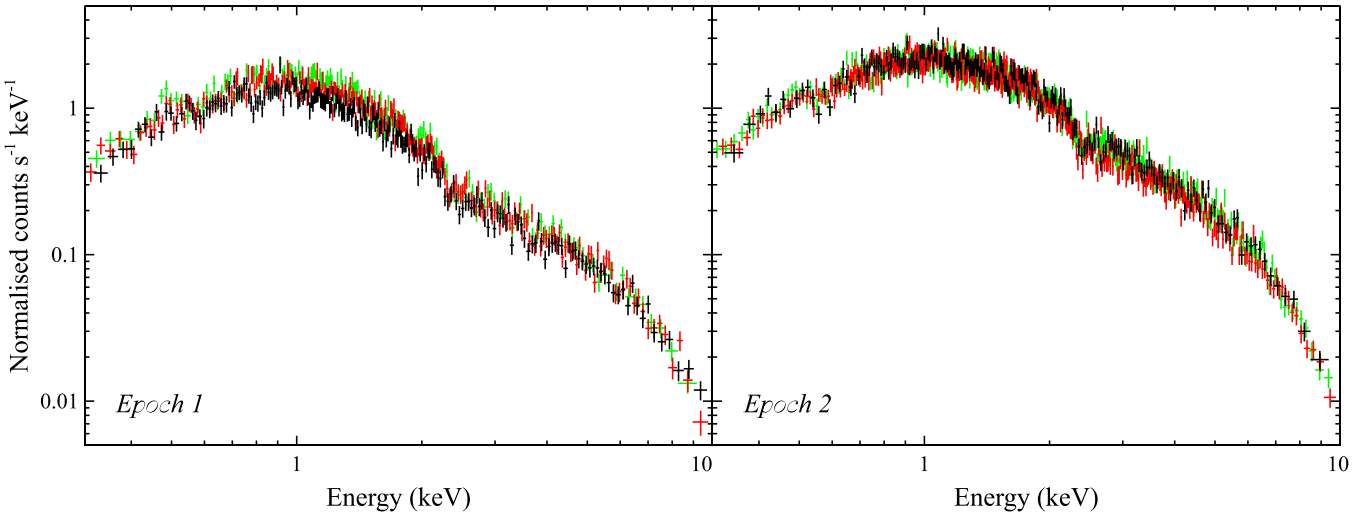

Figure 2. *EPIC*-pn spectra for the two sets of three observations of Holmberg IX X-1, the first taken in October (left panel; associated with *NuSTAR* observation 1) and the second in November (right panel; associated with *NuSTAR* observation 2). The black, red, and green spectra show the first, second, and third observations from each set of three. Although there is some mild flux variability displayed by the observations in each set, it is clear there is very little spectral variability.

(A color version of this figure is available in the online journal.)

v12.8.0 (Arnaud 1996), and quoted uncertainties on spectral parameters are the 90% confidence limits for a single parameter of interest, unless stated otherwise. Neutral absorption is treated with TBNEW,[13] the latest version of the TBABS absorption code (Wilms et al. 2000), with the appropriate solar abundances, and the absorption cross-sections of Verner et al. (1996). All models include Galactic absorption with a column of $N_{\rm H;Gal} = 5.54 \times 10^{20}$ cm^{-2} (Kalberla et al. 2005), in addition to an intrinsic neutral absorber at the redshift of Holmberg IX ($z = 0.000153$) with a column that is free to vary (unless stated otherwise).

3.1. Epoch 1

3.1.1. Cross-Calibration

We focus initially on the data obtained during the first epoch, and first investigate the agreement between the three missions over their common 3–10 keV bandpass, taking this epoch to be representative. We first apply an unabsorbed power-law model to this energy range for each of the three observatories, allowing multiplicative constants to float between the spectra obtained from the various detectors (we choose the constant for *NuSTAR* FPMA to be unity). Although this model formally provides a good fit, with $\chi^2_\nu = 1984/1928$ and $\Gamma_{3-10\,\rm keV} = 1.81^{+0.01}_{-0.02}$, systematic curvature in the residuals can be seen across this bandpass (see Figure 3, top panel). Parameterizing the data with a curved continuum instead, using a simple unabsorbed bremsstrahlung model, provides an excellent fit (Figure 3, bottom panel), with $\chi^2_\nu = 1870/1928$ and $T = 11.0 \pm 0.3$ keV, an improvement of $\Delta\chi^2 = 114$ (for no additional degrees of freedom) over the power-law continuum. Allowing the temperatures to vary independently for each of the different missions does not significantly improve the fit ($\chi^2_\nu = 1861/1926$), and the temperatures obtained all agree within 2σ or better: $T_{\rm XMM} = 12.7^{+1.8}_{-1.3}$ keV, $T_{\rm Suzaku} = 11.1 \pm 0.4$ keV and $T_{\rm NuSTAR} = 10.4 \pm 0.5$ keV. Therefore, we conclude the spectra obtained with *XMM-Newton*, *Suzaku*, and *NuSTAR* show good agreement (see also Walton et al. 2013a; K. K. Madsen et al. 2014; in preparation). The fluxes obtained for each of the different detectors all agree with that of *NuSTAR* FPMA to better than ∼10%.

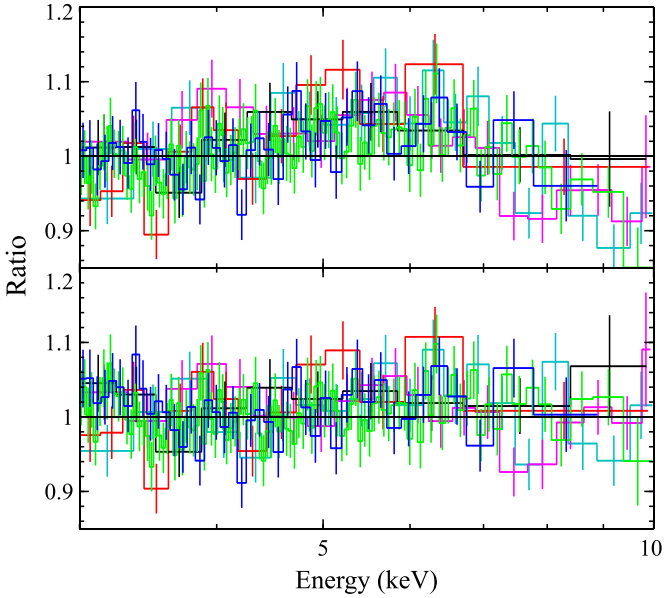

Figure 3. Data/model ratios for the *XMM-Newton* (black: *EPIC*-pn, red: *EPIC*-MOS), *Suzaku* (green: FI XIS, blue: BI XIS), and *NuSTAR* (magenta: FPMA, cyan: FPMB) data sets obtained during epoch 1, modeled with both a power-law continuum (top panel) and a bremsstrahlung continuum (bottom panel). The data from the various missions display consistent curvature across their common energy range (3–10 keV). The data have been rebinned for visual clarity.

(A color version of this figure is available in the online journal.)

Furthermore, the preference for the bremsstrahlung continuum over the power law confirms the presence of curvature in the observed 3–10 keV spectrum, similar to that inferred from earlier *XMM-Newton* data (Stobbart et al. 2006; Gladstone et al. 2009), and from the full *Suzaku* data set (including additional data obtained earlier in 2012; Walton et al. 2013b). The absorption column toward Holmberg IX X-1 is $N_{\rm H} \lesssim 2 \times 10^{21}$ cm^{-2} (e.g., Miller et al. 2013b), which is not sufficient to significantly influence the spectrum in the 3–10 keV bandpass. Thus, the observed curvature must be intrinsic to the 3–10 keV continuum.

[13] http://pulsar.sternwarte.uni-erlangen.de/wilms/research/tbabs

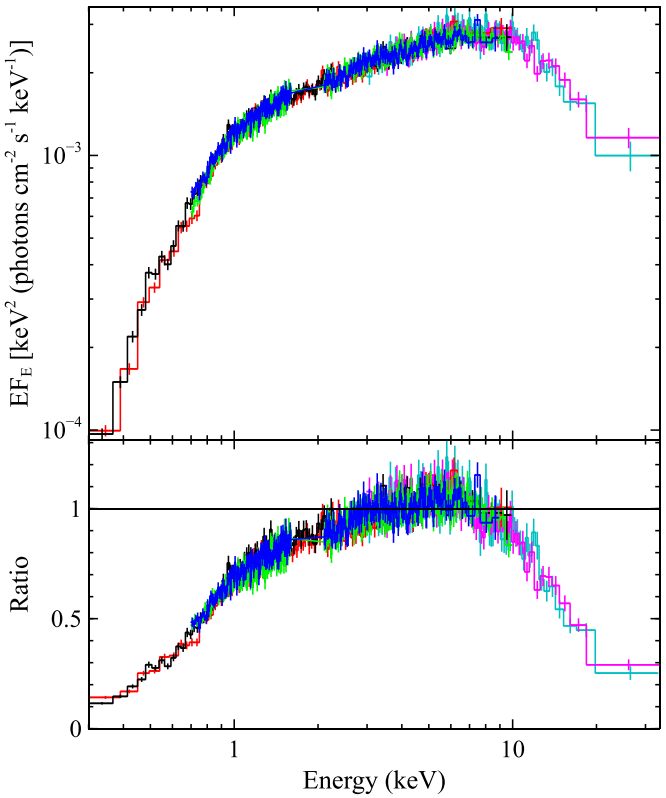

Figure 4. Top panel: the broadband X-ray spectrum displayed by Holmberg IX X-1 during epoch 1. All the data have been unfolded through the same model, which simply consists of a count spectrum that is constant with energy. Bottom panel: data/model ratio to the power-law continuum applied to the 3–10 keV energy range, then extended out to the full broadband spectrum. Both panels clearly demonstrate that the curvature observed in the 3–10 keV bandpass is associated with a true spectral cutoff. The color scheme is the same as for Figure 3, and the data have again been rebinned for clarity.

(A color version of this figure is available in the online journal.)

3.1.2. Broadband Continuum Modelling

We now analyze the full broadband *XMM-Newton* + *Suzaku* + *NuSTAR* spectrum obtained from the first epoch, applying a suite of continuum models in order to examine the nature of the broadband emission from Holmberg IX X-1. Figure 4 (top panel) shows the spectra from epoch 1 unfolded through a model that simply consists of a constant. We also show in Figure 4 (bottom panel) the data/model ratio to the power-law continuum initially applied to the 3–10 keV bandpass (as outlined in Section 3.1.1), then extrapolated across the full 0.3–30.0 keV spectrum considered here.

The *NuSTAR* data clearly show that the curvature displayed in the 3–10 keV bandpass extends to higher energy, and genuinely represents a spectral cutoff, similar to NGC 1313 X-1 (Bachetti et al. 2013) and IC 342 X-1 (Rana et al. 2014). This is contrary to the basic expectation for the interpretation in which the 3–10 keV curvature is produced by relativistic disk reflection with the accretion disk illuminated by a standard sub-Eddington power-law-like corona (Caballero-García & Fabian 2010), as the Compton hump should cause the spectrum to turn back up at higher energies ($\gtrsim$10 keV; Walton et al. 2011a). This model provides a good fit to the data below 10 keV (χ^2_ν = 3419/3360), utilizing the REFLIONX code (Ross & Fabian 2005) for the reflected emission and the RELCONV kernel (Dauser et al. 2010) to account for the relativistic effects inherent to the inner accretion flow around a black hole. However, when

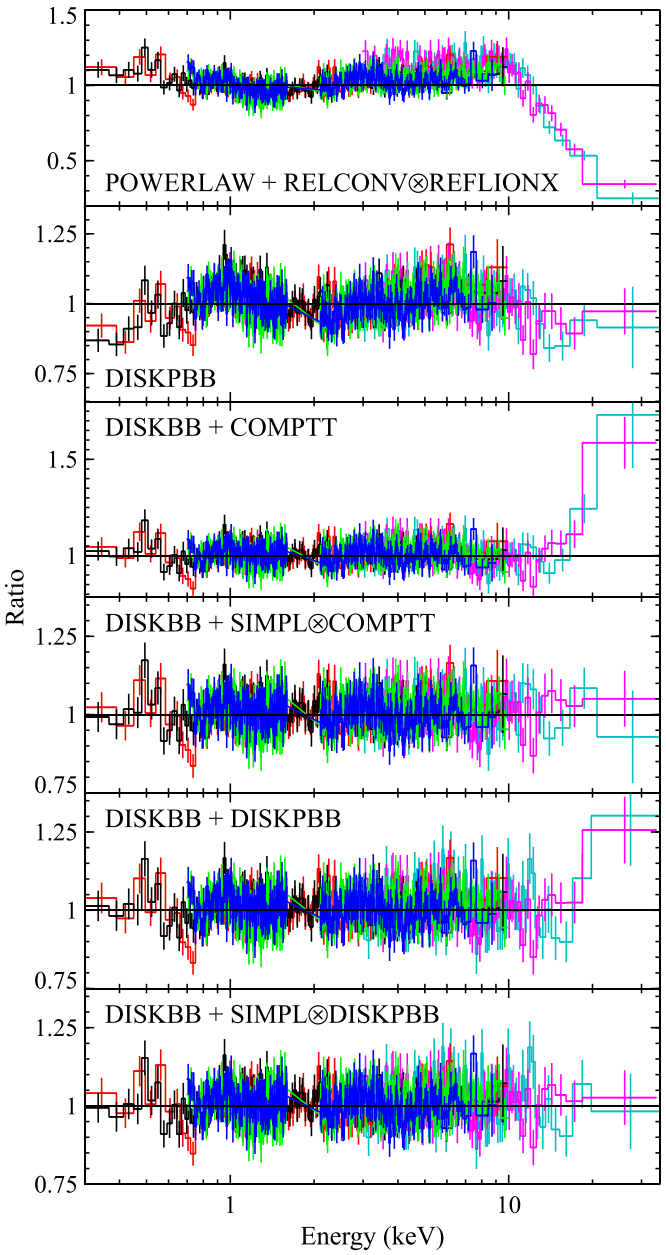

Figure 5. Data/model ratios for a variety of the continuum models applied to the full broadband X-ray spectrum of Holmberg IX X-1 obtained during epoch 1 (see Section 3.1.2). The color scheme is the same as for Figures 3 and 4, and the data have again been rebinned for visual clarity.

(A color version of this figure is available in the online journal.)

applying this model to the full 0.3–30.0 keV bandpass we see that when the curvature is modeled as being due to iron emission, the data are significantly overpredicted at the highest energies (Figure 5), and the resulting broadband fit is poor (χ^2_ν = 6016/3516). We therefore proceed by considering models that invoke a thermal origin for the high energy curvature.

Simple multi-color blackbody accretion disk models (e.g., DISKBB: Mitsuda et al. 1984, DISKPN: Gierliński et al. 1999), assuming a geometrically thin, optically thick disk as per Shakura & Sunyaev (1973), also fail to fit the broadband data (DISKBB: χ^2_ν = 22682/3523; DISKPN: χ^2_ν = 20303/3522). Although the high energy data do show a cutoff similar to a thermal spectrum, the overall profile is too broad to be explained by such simple models. However, at very high- or

Table 2
Best Fit Parameters Obtained for the Variety of Continuum Models Applied to the Broadband Data Available for Holmberg IX X-1

Model	$N_{\rm H;int}$ (10^{21} cm^{-2})	$kT_{\rm in,1}$ (keV)	$kT_{\rm e}$ or $kT_{\rm in,2}$[a] (keV)	p or τ	Γ	$f_{\rm scat}$ (%)	χ^2/DoF
			Epoch 1				
DISKPBB	$1.27^{+0.03}_{-0.04}$	$4.87^{+0.13}_{-0.12}$	...	0.542 ± 0.001	...	...	3913/3522
DISKBB+COMPTT	$1.5^{+0.2}_{-0.3}$	0.15 ± 0.01	3.1 ± 0.1	6.3 ± 0.1	...	...	3651/3520
DISKBB+SIMPL⊗COMPTT	$1.4^{+0.1}_{-0.2}$	0.23 ± 0.04	$2.4^{+0.3}_{-0.4}$	$7.3^{+0.4}_{-0.5}$	>2.4	>16	3581/3518
DISKBB+DISKPBB	1.7 ± 0.1	0.26 ± 0.02	4.2 ± 0.1	$0.560^{+0.004}_{-0.003}$	...	...	3606/3520
DISKBB+SIMPL⊗DISKPBB	1.6 ± 0.1	$0.27^{+0.01}_{-0.02}$	3.8 ± 0.2	0.564 ± 0.004	$1.63^{+0.09}_{-0.08}$	3 ± 1	3584/3518
			Epoch 2				
DISKPBB	1.67 ± 0.06	2.56 ± 0.03	...	0.587 ± 0.004	...	...	2166/1584
DISKBB+COMPTT	0.59 ± 0.04	1.17 ± 0.06	2.7 ± 0.1	$7.1^{+0.7}_{-0.5}$	...	...	1949/1582
DISKBB+SIMPL⊗COMPTT	$1.3^{+0.2}_{-0.1}$	0.3 ± 0.1	$1.11^{+0.06}_{-0.04}$	11.3 ± 0.6	3.6 ± 0.1	>81	1695/1580
DISKBB+DISKPBB	1.7 ± 0.1	1.79 ± 0.04	$5.4^{+0.5}_{-0.4}$	0.514 ± 0.007	...	...	1693/1582
DISKBB+SIMPL⊗DISKPBB	$1.5^{+0.3}_{-0.1}$	$1.63^{+0.07}_{-0.06}$	$3.5^{+0.6}_{-0.3}$	$0.55^{+0.01}_{-0.02}$	<1.65	$2.3^{+0.9}_{-0.6}$	1686/1580

Note. [a] This column gives the temperature of the hotter continuum component, where relevant, i.e., $kT_{\rm e}$ for models including a COMPTT component, or the inner temperature $kT_{\rm in}$ of the DISKPBB component for models invoking both DISKBB and DISKPBB.

super-Eddington rates the accretion disk may differ substantially from the simple Shakura & Sunyaev (1973) thin disk profile owing to the increased effects of radiation pressure and advection (Abramowicz et al. 1988). This can result in shallower radial temperature profiles and the appearance of a broader, less-peaked emission profile from the disk. Allowing the radial temperature profile of the disk (p) to vary as an additional free parameter using the DISKPBB model (Mineshige et al. 1994) does substantially improve the fit ($\chi^2_\nu = 3913/3522$), and the inferred temperature profile is shallower than expected for a thin disk (i.e., $p < 3/4$); the results are presented in Table 2. However, significant structure remains in the residuals (see Figure 5), and the spectrum does appear to require at least two separate continuum components.

We therefore model the broadband spectrum from epoch 1 with the DISKBB+COMPTT combination frequently used to parameterize the spectra from bright ULXs below 10 keV (e.g., Gladstone et al. 2009; Middleton et al. 2011b; Walton et al. 2011a). This model is used to represent a disk–corona accretion geometry, in which hot coronal electrons Compton up-scatter seed photons from the (cooler) accretion disk into a second hard emission component, modeled here with COMPTT (Titarchuk 1994). For simplicity, we require the temperature of the seed photons to be that of the accretion disk component. Although this may not be appropriate if this emission genuinely arises from an optically thick corona (as frequently inferred for ULXs with this model), which may obscure our view of the true inner disk (e.g., Gladstone et al. 2009; Pintore et al. 2014), it is sufficient for our purposes as relaxing this assumption does not improve the fit, nor change the parameter values obtained. The COMPTT model allows both the temperature and the optical depth of the Comptonizing region to be fit as free parameters. This does offer a significant improvement over the simpler DISKPBB model, with $\chi^2_\nu = 3651/3520$, and the results obtained are fairly similar to previous applications of this model to ULX spectra (see Table 2), i.e., the electron plasma is inferred to be fairly cool ($T_{\rm e} \sim 3$ keV) and optically thick ($\tau \sim 6$) owing to the observed spectral curvature in the ∼3–10 keV bandpass, and the seed photon/disk temperature is very cool ($T_{\rm in} \sim 0.15$ keV). However, this model leaves a significant excess at the highest energies probed by *NuSTAR* (see Figure 5), requiring a further high energy continuum component.

Although the DISKBB+COMPTT model formally describes a disk–corona scenario, when applied to ULX spectra the COMPTT component has frequently been interpreted as representing emission from a distorted high-Eddington accretion disk (e.g., Middleton et al. 2011b) rather than standard coronal emission, owing to the large optical depth typically inferred, and the unusually low electron temperatures compared to those observed from standard sub-Eddington coronae (e.g., Gierliński et al. 1999; Miller et al. 2013a; Tomsick et al. 2014; Natalucci et al. 2014; Brenneman et al. 2014). In this scenario, it is therefore plausible that the high energy excess observed represents the true emission from the Comptonizing corona. The addition of a power-law tail to the COMPTT component included in this model, using the SIMPL convolution model (Steiner et al. 2009; limiting the photon index to $1.5 \leqslant \Gamma \leqslant 4$, broadly encompassing the range observed from Galactic binaries), provides a further significant improvement of $\Delta\chi^2 = 70$ (for two additional free parameters) to the fit, and resolves the high energy excess (see Figure 5). Even if poorly constrained owing to a strong degeneracy with the scattered fraction $f_{\rm scat}$ (which serves as the SIMPL "normalization"; see Table 2), the photon index is very steep, $\Gamma > 2.4$. We stress that even though this model still utilizes COMPTT to model the ∼3–10 keV emission, the necessity for a second Comptonizing region at even higher energies strongly suggests that this emission does arise from a hot, super-Eddington disk, which the COMPTT model merely has the flexibility to mimic, rather than physically being associated with an optically thick corona.

Finally, if the high energy emission is dominated by a hot accretion disk, describing this emission with a COMPTT component with the seed photon temperature linked to the soft thermal component might not be correct. We therefore also test other models composed of two thermal components in order to test whether the hard excess observed with the DISKBB+COMPTT combination is simply a consequence of that particular model. A model consisting of two DISKBB components provides a poor fit to the data ($\chi^2_\nu = 4228/3521$), leaving a strong excess in the *NuSTAR* data above 10 keV and substantial residual structure at

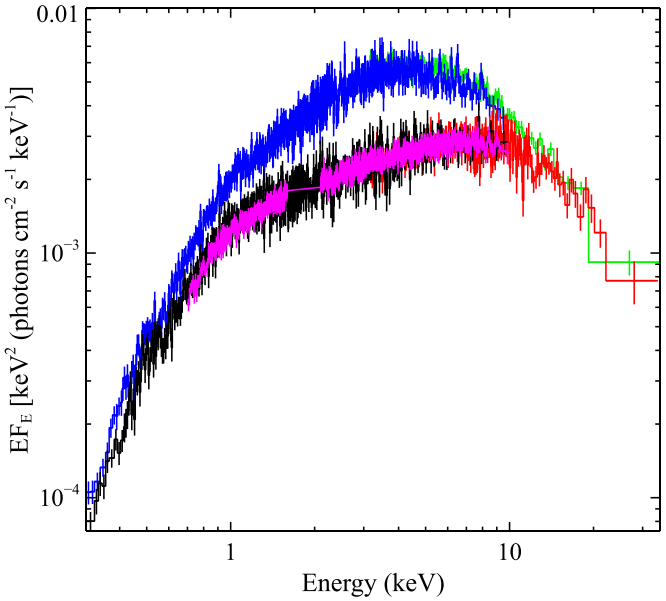

Figure 6. Spectral evolution displayed by Holmberg IX X-1 between the two epochs. The *XMM-Newton* (*EPIC*-pn), *Suzaku* (FI XIS), and *NuSTAR* (FPMA) data from epoch 1 are shown in black, magenta, and red, respectively, while the *XMM-Newton* and *NuSTAR* data from epoch 2 are shown in blue and green. All the data have been unfolded through the same model, which again consists of a constant.

(A color version of this figure is available in the online journal.)

Table 3
Observed Fluxes for Holmberg IX X-1[4]

Epoch	Fluxes (10^{-12} erg cm^{-2} s^{-1})		
	(0.3–10.0 keV)	(10.0–30.0 keV)	(0.3–30.0 keV)
1	9.8 ± 0.1	2.8 ± 0.1	12.6 ± 0.2
2	19.2 ± 0.2	3.0 ± 0.1	22.2 ± 0.2

lower energies. Replacing the second (hotter) DISKBB with a DISKPBB component, with the radial temperature profile free to vary again provides a significant improvement ($\chi^2_\nu = 3606/3520$). However, there is still evidence for an excess remaining at the highest energies (see Figure 5); the addition of SIMPL here gives an improvement of $\Delta\chi^2 = 22$ (for two additional free parameters). Although the best fit photon index of the power-law tail is rather hard in this case, we note that there is a local minimum of similar statistical quality ($\chi^2_\nu = 3588/3518$) with a steep photon index ($\Gamma > 3.1$). Furthermore, even in the model with the hard photon index, the hard power-law continuum only begins to dominate the model outside of the bandpass probed. Within the *NuSTAR* bandpass, the effect is still to append a steep tail onto the DISKPBB component, similar to the case with the steep photon index, as the model begins to curve up into the hard portion of this continuum. It seems that the marginal preference for a hard photon index arises from the subtle difference this model has on the curvature at lower energies, rather than the slope of the *observed* continuum above ~15 keV, which Figure 4 shows is steep.

3.2. Epoch 2

During the second epoch, Holmberg IX X-1 was substantially brighter than during the first epoch (see Table 3). Although there is no evidence for substantial spectral variability during either of the two epochs, the spectra from the two epochs do exhibit marked differences, as shown in Figure 6. The strongest variability can clearly be seen at ~3 keV, and the 3–10 keV spectrum now appears to be more peaked than during epoch 1. In contrast, however, there is remarkably little variability in the spectrum at the highest ($\gtrsim$15 keV) and the lowest ($\lesssim$1 keV) energies. One of the thermal components required in epoch 1 appears to have evolved substantially both in terms of its temperature and its flux, while the other appears to have remained relatively stable.

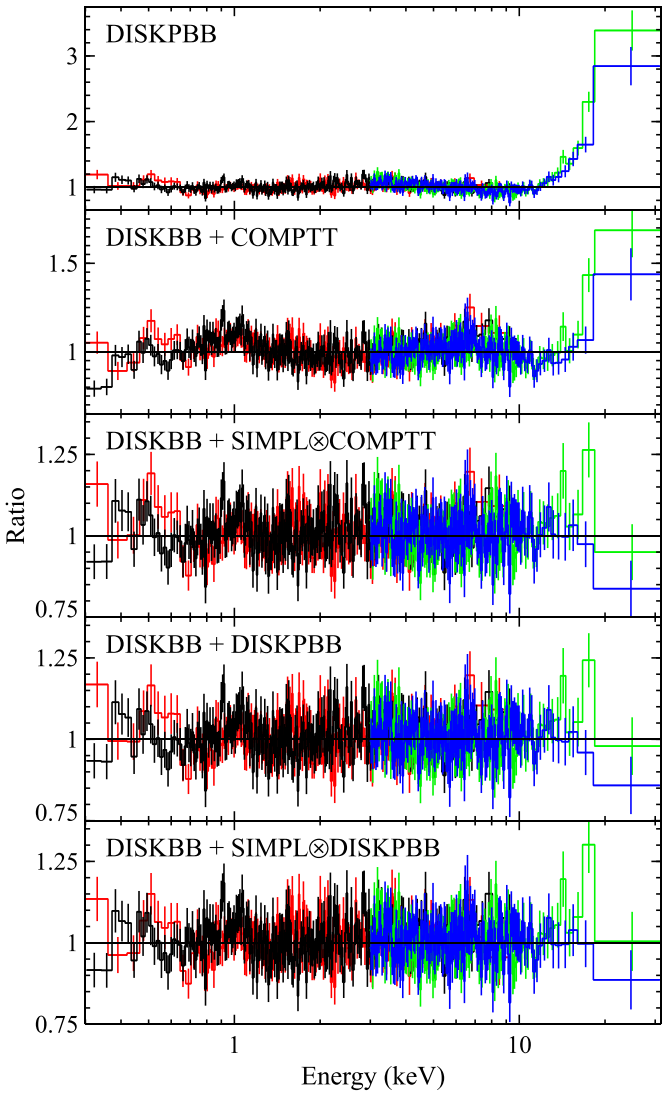

Figure 7. Data/model ratios for a variety of the continuum models applied to the full broadband X-ray spectrum of Holmberg IX X-1 obtained during epoch 2 (see Section 3.2). *XMM-Newton EPIC*-pn and *EPIC*-MOS data are shown in black and red, respectively, and *NuSTAR* FPMA and FPMB in green and blue; the data have been rebinned for visual clarity.

(A color version of this figure is available in the online journal.)

We therefore apply the thermal models considered for epoch 1 to these data, in order to investigate which of these can adequately reproduce the epoch 2 spectrum. Even though the spectrum now appears to be primarily dominated by one of the thermal components, simple accretion disk models still fail to adequately reproduce the data; an absorbed DISKBB model gives a very poor fit, with $\chi^2_\nu = 4727/1585$. Allowing the radial temperature profile to vary again substantially improves the fit ($\chi^2_\nu = 2166/1584$), but the data still show a strong excess over the model at the highest energies, and at least two continuum components still appear to be required for this epoch (see Figure 7).

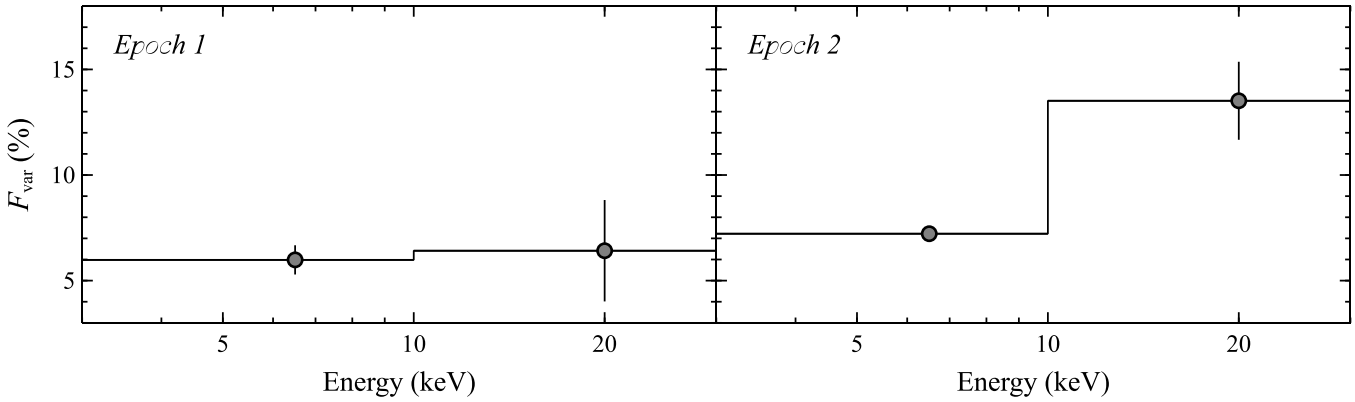

Figure 8. Fractional excess variability ($F_{\rm var}$; covering frequencies 1.4×10^{-5} to 10^{-3} Hz, i.e., 5–70 ks timescales) above and below 10 keV observed from Holmberg IX X-1 with *NuSTAR* during the two epochs (see Section 4). There is tentative evidence for enhanced variability above 10 keV in the second epoch.

We therefore fit the DISKBB+COMPTT model considered previously. While the fit is improved over the DISKPBB model, it is still relatively poor ($\chi^2_\nu = 1949/1582$), and the high energy excess persists, even though in this model it is the DISKBB component that shifts up in temperature to try and account for the peak of the emission (at ∼4 keV; Figure 6), while the best fit temperature and the optical depth for the COMPTT component are similar to the first epoch (see Table 2). Allowing again for a further high energy power-law tail to the COMPTT component with SIMPL substantially improves the fit ($\chi^2_\nu = 1695/1580$), and accounts for the high energy excess. However, the best fit results are very different to those obtained with the simpler DISKBB+COMPTT model. Now it is the DISKBB component that appears to have remained fairly constant, while the COMPTT component has decreased its temperature and increased its flux to account for the ∼4 keV peak. Other aspects have remained similar to the first epoch though, and the COMPTT component is again inferred to be optically thick ($\tau \sim 11$).

Finally, we also reconsider the DISKBB+DISKPBB model applied previously to the first epoch. This model provides a similar quality fit to the DISKBB+COMPTT+SIMPL combination ($\chi^2_\nu = 1693/1582$), but here it is the DISKPBB component which primarily accounts for the high energy emission, while the temperature of the DISKBB component has increased substantially to account for the ∼4 keV spectral peak (again, see Table 2). In contrast to the first epoch, adding a high energy power-law tail to the DISKPBB component only provides a marginal improvement to the fit ($\chi^2_\nu = 1686/1580$). Furthermore, we note that as with the first epoch, even though the best fit photon index is rather hard, this portion of the continuum again only dominates outside of the observed bandpass, and the observed continuum at the highest energies probed is still actually very steep, as is clear from Figure 6.

4. SHORT-TERM VARIABILITY

We also investigate the short-term variability behavior during these epochs. In order to crudely assess how the variability may evolve with energy, we produce light curves over the energy ranges 3–10 and 10–30 keV for each of the *NuSTAR* observations, and estimate the fractional excess variability ($F_{\rm var}$; Edelson et al. 2002; Vaughan et al. 2003) for each energy band for the two epochs. In order to ensure the same timescales are probed during each epoch, we split the light curves into ∼70 ks segments, calculate $F_{\rm var}$ for each and compute the weighted average. We use 70 ks segments as this is roughly the duration of the last part of the second observation, and it divides the first observation neatly into three segments. As the central part of observation 2 does not span sufficient duration, these data are not considered here, and we only utilize the first 70 ks of the first part. In order to ensure the variability above 10 keV is not dominated by Poisson noise, we again use time bins of 5 ks. The results are shown in Figure 8. During the first epoch, mild variability is observed, which seems to be constant with energy. However, during the second epoch, while the variability below 10 keV is broadly consistent with the level displayed during the first, we see some evidence for enhanced variability above 10 keV, both in comparison to the variability below 10 keV during this epoch, and the variability observed during the first epoch.

5. DISCUSSION

We have presented an analysis of the broadband X-ray spectrum of the extreme ULX Holmberg IX X-1, observed twice during 2012, by *NuSTAR*, *XMM-Newton*, and *Suzaku*. *NuSTAR* has provided the first high quality hard X-ray ($E > 10$ keV) spectra of this remarkable source to date. During both epochs the hard X-ray emission is weak in comparison to the soft X-ray ($E < 10$ keV) emission, as demonstrated by the fluxes presented in Table 3; the flux above 10 keV represents at most ∼25% of the full 0.3–30.0 keV flux observed during either epoch. The observed 0.3–30.0 keV X-ray luminosities from the two epochs (assuming isotropy and before any absorption corrections) are $L_{\rm X,1} = (1.90\pm0.03)\times10^{40}$ erg s^{-1} and $L_{\rm X,2} = (3.35\pm0.03)\times10^{40}$ erg s^{-1}, for a distance to Holmberg IX of 3.55 Mpc (Paturel et al. 2002). Correcting for the absorption column inferred from our spectral analysis[14] (Table 2), these correspond to intrinsic 0.3–30.0 keV luminosities of $L_{\rm int,1} = (2.21\pm0.05)\times10^{40}$ erg s^{-1} and $L_{\rm int,2} = (3.91\pm0.08)\times10^{40}$ erg s^{-1}.

The *NuSTAR* data confirm that the curvature observed previously in the 3–10 keV bandpass (e.g., Stobbart et al. 2006; Gladstone et al. 2009; Walton et al. 2013b) is a genuine spectral cutoff, as is suggested by the weak *INTEGRAL* detection presented by Sazonov et al. (2013). This is also similar to the results observed from other extreme ($L_{\rm X} \gtrsim 10^{40}$ erg s^{-1}) ULXs observed by *NuSTAR* to date, e.g., Circinus ULX5 (Walton et al. 2013a), NGC 1313 X-1 (Bachetti et al. 2013), and IC 342 X-1

[14] We use the DISKBB+SIMPL⊗COMPTT model to calculate fluxes, but note that the models using DISKPBB instead of COMPTT give equivalent fits, and similar absorption columns are obtained.

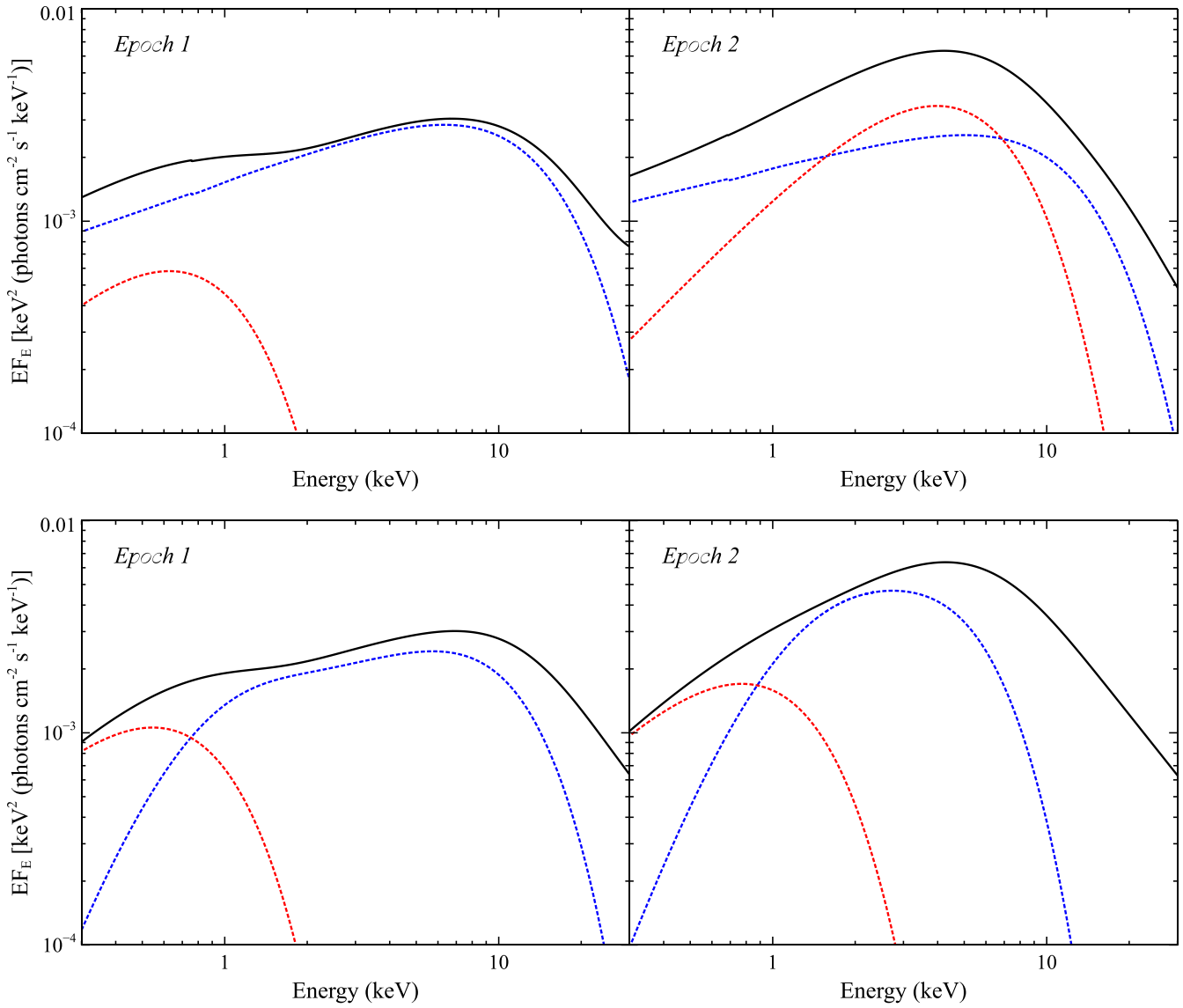

Figure 9. Top panels: the relative contribution of the various spectral components inferred with the DISKBB+SIMPL⊗DISKPBB model (corrected for absorption) for each epoch. The full model is shown in black, while the DISKBB contribution is shown in red, and the DISKPBB contribution (before modification by SIMPL) is shown in blue. In this case, the spectral evolution is dominated by the cooler of the two thermal components (represented by DISKBB). Bottom panels: the same as the top panels, but for the DISKBB+SIMPL⊗COMPTT model. Here, the DISKBB contribution is shown in red, and the COMPTT contribution (before modification by SIMPL) is shown in blue. In this case, the spectral evolution is dominated by the hotter of the two thermal components (represented by COMPTT).

(A color version of this figure is available in the online journal.)

(Rana et al. 2014). Indeed, the broadband spectrum of Holmberg IX X-1 from the first epoch is remarkably similar to the latter two sources. Neither epoch is consistent with emission from the standard low/hard state commonly exhibited by Galactic BHBs (see Remillard & McClintock 2006), as would broadly have been expected if Holmberg IX X-1 were an IMBH accreting at substantially sub-Eddington accretion rates, under the assumption that the accretion geometry is independent of black hole mass. It therefore seems likely that we are viewing an unusual high-Eddington phase of accretion, the physics of which we are only just beginning to probe.

During each epoch, the spectra appear to be best described with a combination of two thermal components, potentially with a power-law-like tail present at the highest energies observed, although the contribution of this latter component is somewhat model dependent. In both epochs, one of these components is consistent with being a standard thin accretion disk (Shakura & Sunyaev 1973), although the second (hotter) thermal component deviates from this independent of the inclusion of a high energy tail. The hotter component can be modeled with either an optically thick thermal Comptonization model (which strongly requires the additional high energy power-law-like tail), or a multi-color blackbody disk model in which the radial temperature profile deviates from that expected from a simple thin disk. If an additional power-law-like emission component truly is present at the highest energies probed, it generally appears to be very steep (see Figure 9), potentially similar to the very high/steep power-law state exhibited by Galactic BHBs at relatively high accretion rates (Remillard & McClintock 2006).

Two component thermal models could plausibly represent a variety of scenarios. The cooler DISKBB could be standard disk emission (see also Miller et al. 2013b) from the outer accretion flow, while the hotter, nonstandard thermal component could arise from the inner disk where the effects of radiation pressure are the most prominent, and drive the disk structure away from

the standard thin disk scenario (e.g., Abramowicz et al. 1988). Alternatively, the soft thermal component could be emission from the photosphere of a massive optically thick outflow (e.g., Middleton et al. 2011a; Sutton et al. 2013), which may display some similarity to standard disk emission, with the hotter emission again arising in the distorted inner disk, broadly similar to the picture for high/super-Eddington accretion proposed by Poutanen et al. (2007); see also Dotan & Shaviv (2011) and Ohsuga & Mineshige (2011).

Alternatively, Dexter & Quataert (2012) proposed a framework in which the surface of the disk is inhomogeneous, resulting in surface temperature fluctuations and thus deviations in the relative contribution of the emission at different temperatures from the simple thin disk approximation. Such inhomogeneities could potentially result in a highly distorted thermal spectrum, and might possibly be able to simultaneously explain both of the thermal components required to model the observed spectra, as suggested in the context of ULXs by Miller et al. (2013b, 2014). As discussed in Miller et al. (2014), such inhomogeneities could arise naturally through the "photon-bubble" instability (e.g., Gammie 1998; Begelman 2002), which may play an important role in high-Eddington accretion flows.

Finally, we stress again that while the hotter component has also previously been interpreted as an optically thick corona (e.g., Gladstone et al. 2009; Pintore et al. 2014), the necessity for an additional Comptonizing continuum at higher energies with such a model renders such a physical interpretation highly unlikely, and favors the hot, inner accretion disk scenarios outlined above.

5.1. Spectral Variability

The most striking aspect of these broadband observations is the spectral variability observed between the two epochs (see Figure 6). In the second epoch, Holmberg IX X-1 was observed in a much brighter state, in which both the temperature and the flux of one of the two thermal components appears to have changed significantly in comparison to the first. However, as the emission at the lowest ($E \lesssim 1$ keV) and the highest ($E \gtrsim 10$ keV) energies observed has remained remarkably constant in comparison to the intermediate energies, we find that this evolution can be equally well described as the low temperature component increasing both its temperature (from ~0.3 to ~1.5 keV) and flux while the high temperature component remains broadly stable (case 1), and as the high temperature component decreasing its temperature (from ~4 to ~1.5 keV) and increasing its flux while the low temperature component remains broadly stable (case 2). The latter case strongly requires the additional presence of a high energy power-law tail, while the picture is less clear cut for the former, with the addition of such a component providing a reasonable improvement to the fit in the first epoch, but only a marginal improvement in the second (see Sections 3.1.2 and 3.2). These two evolutionary scenarios are shown in Figure 9, represented by the DISKBB+SIMPL⊗DISKPBB and DISKBB+SIMPL⊗COMPTT models from each epoch respectively.[15]

Case 1 requires the flux and the temperature of the evolving emission component to be positively correlated, as broadly expected for thermal emission. However, the observed evolution would have to deviate strongly from the $L \propto T^4$ relation expected for simple blackbody emission with a constant emitting area, as would be expected for a stable, geometrically thin disk. Instead, the temperatures and fluxes obtained in case 1 imply the evolution would have to follow a much flatter, almost linear relation, i.e., $L \propto T$. In contrast, the results for case 2 imply an anti-correlation between the temperature and the flux of the evolving component, opposite to the basic expectation for thermal emission, and is therefore challenging to explain.

Considering first case 1 (i.e., the lower temperature component dominating the evolution), our recent analysis of the extreme ULX Circinus ULX5 also found a luminosity–temperature relation significantly flatter than the basic expectation for blackbody emission (in that case, $L \propto T^{1.7}$; Walton et al. 2013a), although the deviation from $L \propto T^4$ in Circinus ULX5 was not as extreme as inferred here. As discussed in that work, a shallow L–T relation would imply either that the inner radius of the disk decreases with increasing luminosity (geometric changes), or that the color correction factor ($f_{\rm col}$, which relates the observed surface temperature of the disk to the effective blackbody temperature via $T_{\rm in} = f_{\rm col} T_{\rm eff}$) increases with increasing luminosity (atmospheric changes). For Circinus ULX5, the latter scenario is preferred, due to its high luminosity.

However, in the case of Circinus ULX5, the identification of the thermal component as emission from the inner disk is likely robust, as the high energy emission was well explained as Comptonization in an optically thin corona. For Holmberg IX X-1, this is certainly not the case, and the higher energy emission instead appears to be dominated by a second thermal emission component in this scenario (see Figure 9), seemingly associated with optically thick material. Given its higher temperature, it is natural to assume this material represents the inner disk, and thus that the cooler emission arises from farther out. This association is supported by the failure of models that associate this emission with the Comptonizing corona; optically thin coronal emission is strongly ruled out, and optically thick coronal emission in turn ends up strongly requiring a second, steep Comptonized continuum in the *NuSTAR* bandpass. Furthermore, recent work by Tao & Blaes 2013 suggest hot, luminous accretion disks may naturally produce such tails.

Given the stability inferred for the high temperature emission in this scenario, a strong wind may be required to remove the fluctuations observed in the cooler, more distant regions before they propagate through to the inner flow. In order to efficiently dampen out these fluctuations, the wind would most likely have to remove a very large fraction of the accreted mass at the point it is launched, particularly at higher luminosities. This evolutionary scenario could be considered broadly similar to certain aspects of those proposed in Sutton et al. (2013) and Pintore et al. (2014), who associate the soft component with emission from a large outflow, and suggest that as the accretion rate increases the emission from this component should become more prominent, although as discussed previously this interpretation of the soft emission is not unique (Miller et al. 2014). We note that unambiguous signatures of such an outflow in the form of the ionized iron K α absorption features associated with disk winds in Galactic binaries are not observed in Holmberg IX X-1 (Walton et al. 2012, 2013b), suggesting either such outflows are absent, or directed away from us such that they do not obscure our line-of-sight to the inner accretion flow.

Recently Middleton et al. (2014) investigated atomic features in the iron-L bandpass (~1 keV) for two luminous ULXs with soft X-ray spectra, NGC 5408 X-1 and NGC 6946 X-

[15] Although for the latter model the statistical requirement for the SIMPL component is not strictly significant for the second epoch (see Section 3.2), we show this model for direct comparison with the first epoch.

1, suggesting that these features could be explained, at least in part, by broad absorption features associated with an outflow. On inspection, there is a tentative suggestion of the presence of residual features at similar energies here, particularly during the second epoch. However, if real, it is unlikely they are absorption features in this case, given the lack of accompanying iron K α absorption features (see above) which are predicted by the models generated in Middleton et al. (2014), implying an emission origin instead. It is interesting to note that if the residuals from the second, brighter epoch (see $\sim$1 keV in Figure 7) are interpreted as atomic emission (e.g., emission from a thermal plasma), the strength of the emission must vary from epoch to epoch, apparently in response to the ULX continuum emission. Thus, they would have to be associated with the ULX rather than with steady diffuse emission. However, the exact profile of the residuals from the two epochs is not always consistent for each of the operational detectors, so any physical interpretation must be treated with caution, as the residuals may simply relate to calibration uncertainties. Observations with the high-resolution *Astro-H* micro-calorimeter (Takahashi et al. 2012) will be required to robustly address this issue as there is insufficient signal in the RGS spectra; currently there is no clear X-ray atomic evidence for the presence of an outflow in Holmberg IX X-1.

For case 2 (the hotter component dominating the evolution), the anti-correlation between luminosity and temperature is even more counter-intuitive for thermal blackbody emission than the shallow correlation required for the first scenario. However, the short term variability behavior (see Section 4) may offer some independent support for this evolutionary scenario. In this case, the need for an additional high energy power-law-like tail to the hotter component is very strong. As the hotter component decreases in temperature, this high energy tail makes a more substantial contribution to the spectrum in the 0.3–30.0 keV bandpass, contributing initially only at the very highest energies in the first epoch, and then dominating the emission above 10 keV in the second (see Figure 9). Simultaneously, we see evidence for an increase in the short-term variability above 10 keV during the second epoch (Figure 8).

In Galactic BHBs, short-term variability is generally associated with strong coronal emission (e.g., Churazov et al. 2001; Homan et al. 2001); harder states dominated by the coronal emission generally display stronger variability than disk-dominated soft states, and in intermediate states the variability is generally strongest at the energies at which the corona dominates. In contrast, since the spectral evolution would be dominated by the low-energy component in case 1, with the high energy emission remaining stable, one might not expect to see any evolution in the short-term variability properties at high energies in this scenario. Furthermore, it is interesting to note that the latest high-Eddington accretion disk models being generated may actually predict a regime at the highest accretion rates in which the luminosity and temperature inferred for the disk display an anti-correlation (Bursa et al. 2014, in preparation). If these models are correct, and the spectral evolution displayed by Holmberg IX X-1 is truly described by this second scenario, the implication is that Holmberg IX X-1 is accreting at a very high accretion rate on the Eddington scale.

Determining the origin and the nature of this spectral evolution is important for furthering our understanding of the nature of the accretion onto Holmberg IX X-1, and how the physical structure of the accretion flow might evolve. However, the two broad evolutionary scenarios allowed by the current broadband observations do not appear to be obviously distinguished on physical grounds; both require highly nonstandard behavior, which could nevertheless be considered plausible under certain circumstances. Further broadband observations probing a more diverse range of flux states will be required to determine the true origin of the remarkable evolution displayed by Holmberg IX X-1.

6. CONCLUSIONS

We have presented results from the coordinated broadband X-ray observations of the extreme ULX Holmberg IX X-1 performed by *NuSTAR*, *XMM-Newton* and *Suzaku* in late 2012. The *NuSTAR* detections provide the first high-quality spectra of Holmberg IX X-1 at hard X-rays to date, extending our X-ray coverage up to $\sim$30–35 keV. Observations were undertaken during two epochs, between which Holmberg IX X-1 exhibited strong spectral variability. Neither epoch is consistent with emission from the standard low/hard accretion state, as would have been expected if Holmberg IX X-1 harbors an IMBH accreting at substantially sub-Eddington rates; the *NuSTAR* data confirm in each case that the curvature observed previously in the 3–10 keV bandpass is a true spectral cutoff. Instead, the spectrum appears to be dominated by two optically thick thermal components, likely associated with a distorted accretion disk, with a nonthermal tail also potentially detected at the highest energies probed. The data allow for either of the two thermal components to dominate the spectral evolution, although we find that both scenarios require highly nonstandard behavior for behavior for thermal accretion disk emission. Further broadband observations covering a broader range of fluxes will be required to determine which component is truly dominating the observed evolution.

The authors would like to thank the referee for providing useful feedback, which helped to improve the manuscript. This research has made use of data obtained with the *NuSTAR* mission, a project led by the California Institute of Technology (Caltech), managed by the Jet Propulsion Laboratory (JPL) and funded by NASA, *XMM-Newton*, an ESA science mission with instruments and contributions directly funded by ESA Member States and NASA, and *Suzaku*, a collaborative mission between the space agencies of Japan (JAXA) and the USA (NASA). We thank the *NuSTAR* Operations, Software, and Calibration teams for support with the execution and analysis of these observations. This research was supported under NASA grant No. NNG08FD60C, and has made use of the *NuSTAR* Data Analysis Software (NUSTARDAS), jointly developed by the ASI Science Data Center (ASDC, Italy) and Caltech (USA). We also made use of the NASA/IPAC Extragalactic Database (NED), which is operated by JPL, Caltech, under contract with NASA. Many of the figures included in this work have been produced with the Veusz plotting package: http://home.gna.org/veusz, written and maintained by Jeremy Sanders. DB and MB are grateful to the Centre National d'Etudes Spatiales (CNES) for funding their activities.

Facilites: NuSTAR, *XMM*, *Suzaku*

REFERENCES

Abramowicz, M. A., Czerny, B., Lasota, J. P., & Szuszkiewicz, E. 1988, ApJ, 332, 646

Arnaud, K. A. 1996, in ASP Conf. Ser. 101, Astronomical Data Analysis Software and Systems V, ed. G. H. Jacoby & J. Barnes (San Francisco, CA: ASP), 17

Bachetti, M., Rana, V., Walton, D. J., et al. 2013, ApJ, 778, 163
Begelman, M. C. 2002, ApJL, 568, L97
Berghea, C. T., Dudik, R. P., Weaver, K. A., & Kallman, T. R. 2010, ApJ, 708, 364
Brenneman, L. W., Madejski, G., Fuerst, F., et al. 2014, ApJ, 781, 83
Caballero-García, M. D., & Fabian, A. C. 2010, MNRAS, 402, 2559
Churazov, E., Gilfanov, M., & Revnivtsev, M. 2001, MNRAS, 321, 759
Dauser, T., Wilms, J., Reynolds, C. S., & Brenneman, L. W. 2010, MNRAS, 409, 1534
Dexter, J., & Quataert, E. 2012, MNRAS, 426, L71
Dotan, C., & Shaviv, N. J. 2011, MNRAS, 413, 1623
Edelson, R., Turner, T. J., Pounds, K., et al. 2002, ApJ, 568, 610
Farrell, S. A., Webb, N. A., Barret, D., Godet, O., & Rodrigues, J. M. 2009, Natur, 460, 73
Feng, H., & Soria, R. 2011, NAR, 55, 166
Finke, J. D., & Böttcher, M. 2007, ApJ, 667, 395
Gammie, C. F. 1998, MNRAS, 297, 929
Gierliński, M., Zdziarski, A. A., Poutanen, J., et al. 1999, MNRAS, 309, 496
Gladstone, J. C., Roberts, T. P., & Done, C. 2009, MNRAS, 397, 1836
Harrison, F. A., Craig, W. W., Christensen, F. E., et al. 2013, ApJ, 770, 103
Homan, J., Wijnands, R., van der Klis, M., et al. 2001, ApJS, 132, 377
Jonker, P. G., Heida, M., Torres, M. A. P., et al. 2012, ApJ, 758, 28
Kalberla, P. M. W., Burton, W. B., Hartmann, D., et al. 2005, A&A, 440, 775
Kong, A. K. H., Yang, Y. J., Yen, T.-C., Feng, H., & Kaaret, P. 2010, ApJ, 722, 1816
Koyama, K., Tsunemi, H., Dotani, T., et al. 2007, PASJ, 59, 23
Liu, J.-F., Bregman, J. N., Bai, Y., Justham, S., & Crowther, P. 2013, Natur, 503, 500
Markoff, S., Nowak, M., Young, A., et al. 2008, ApJ, 681, 905
Middleton, M. J., Miller-Jones, J. C. A., Markoff, S., et al. 2013, Natur, 493, 187
Middleton, M. J., Roberts, T. P., Done, C., & Jackson, F. E. 2011a, MNRAS, 411, 644
Middleton, M. J., Sutton, A. D., & Roberts, T. P. 2011b, MNRAS, 417, 464
Middleton, M. J., Walton, D. J., Roberts, T. P., & Heil, L. 2014, MNRAS, 438, 51
Miller, J. M., Bachetti, M., Barret, D., et al. 2014, ApJL, 785, L7
Miller, J. M., Fabbiano, G., Miller, M. C., & Fabian, A. C. 2003, ApJL, 585, L37
Miller, J. M., Nowak, M., Markoff, S., Rupen, M. P., & Maitra, D. 2010, ApJ, 720, 1033
Miller, J. M., Parker, M. L., Fuerst, F., et al. 2013a, ApJL, 775, L45
Miller, J. M., Raymond, J., Fabian, A. C., et al. 2004, ApJ, 601, 450
Miller, J. M., Walton, D. J., King, A. L., et al. 2013b, ApJL, 776, L36
Mineshige, S., Hirano, A., Kitamoto, S., Yamada, T. T., & Fukue, J. 1994, ApJ, 426, 308
Mitsuda, K., Bautz, M., Inoue, H., et al. 2007, PASJ, 59, 1
Mitsuda, K., Inoue, H., Koyama, K., et al. 1984, PASJ, 36, 741
Moon, D.-S., Harrison, F. A., Cenko, S. B., & Shariff, J. A. 2011, ApJL, 731, L32
Natalucci, L., Tomsick, J. A., Bazzano, A., et al. 2014, ApJ, 780, 63
Ohsuga, K., & Mineshige, S. 2011, ApJ, 736, 2
Orosz, J. A. 2003, in IAU Symp. 212, A Massive Star Odyssey: From Main Sequence to Supernova, ed. K. van der Hucht, A. Herrero, & C. Esteban (Cambridge: Cambridge Univ. Press), 365
Paturel, G., Theureau, G., Fouqué, P., et al. 2002, A&A, 383, 398
Pintore, F., Zampieri, L., Wolter, A., & Belloni, T. 2014, MNRAS, 439, 3461
Poutanen, J., Lipunova, G., Fabrika, S., Butkevich, A. G., & Abolmasov, P. 2007, MNRAS, 377, 1187
Rana, V., Harrison, F. A., Bachetti, M., et al. 2014, ApJ, submitted (arXiv:1401.4637)
Remillard, R. A., & McClintock, J. E. 2006, ARA&A, 44, 49
Roberts, T. P. 2007, Ap&SS, 311, 203
Ross, R. R., & Fabian, A. C. 2005, MNRAS, 358, 211
Sazonov, S., Lutovinov, A., & Krivonos, R. 2014, AstL, 40, 65
Shakura, N. I., & Sunyaev, R. A. 1973, A&A, 24, 337
Steiner, J. F., Narayan, R., McClintock, J. E., & Ebisawa, K. 2009, PASP, 121, 1279
Stobbart, A.-M., Roberts, T. P., & Wilms, J. 2006, MNRAS, 368, 397
Strohmayer, T. E., & Mushotzky, R. F. 2009, ApJ, 703, 1386
Strüder, L., Briel, U., Dennerl, K., et al. 2001, A&A, 365, L18
Sutton, A. D., Roberts, T. P., & Middleton, M. J. 2013, MNRAS, 435, 1758
Sutton, A. D., Roberts, T. P., Walton, D. J., Gladstone, J. C., & Scott, A. E. 2012, MNRAS, 423, 1154
Swartz, D. A., Soria, R., Tennant, A. F., & Yukita, M. 2011, ApJ, 741, 49
Takahashi, T., Abe, K., Endo, M., et al. 2007, PASJ, 59, 35
Takahashi, T., Mitsuda, K., Kelley, R., et al. 2012, Proc. SPIE, 8443
Tao, T., & Blaes, O. 2013, ApJ, 770, 55
Titarchuk, L. 1994, ApJ, 434, 570
Tomsick, J. A., Nowak, M. A., Parker, M., et al. 2014, ApJ, 780, 78
Turner, M. J. L., Abbey, A., Arnaud, M., et al. 2001, A&A, 365, L27
Vaughan, S., Fabian, A. C., & Nandra, K. 2003, MNRAS, 339, 1237
Verner, D. A., Ferland, G. J., Korista, K. T., & Yakovlev, D. G. 1996, ApJ, 465, 487
Vierdayanti, K., Done, C., Roberts, T. P., & Mineshige, S. 2010, MNRAS, 403, 1206
Walton, D. J., Fuerst, F., Harrison, F., et al. 2013a, ApJ, 779, 148
Walton, D. J., Gladstone, J. C., Roberts, T. P., et al. 2011a, MNRAS, 414, 1011
Walton, D. J., Miller, J. M., Harrison, F. A., et al. 2013b, ApJL, 773, L9
Walton, D. J., Miller, J. M., Reis, R. C., & Fabian, A. C. 2012, MNRAS, 426, 473
Walton, D. J., Nardini, E., Fabian, A. C., Gallo, L. C., & Reis, R. C. 2013c, MNRAS, 428, 2901
Walton, D. J., Roberts, T. P., Mateos, S., & Heard, V. 2011b, MNRAS, 416, 1844
Wilms, J., Allen, A., & McCray, R. 2000, ApJ, 542, 914
Zampieri, L., & Roberts, T. P. 2009, MNRAS, 400, 677